Applied Surface Science 601 (2022) 154292

Contents lists available at ScienceDirect

Applied Surface Science

journal homepage: www.elsevier.com/locate/apsusc

Full Length Article

Investigation on isopropanol sensing properties of $LnFeO_3$(Ln = Nd, Dy, Er) perovskite materials synthesized by microwave-assisted hydrothermal method

Hongfeng Chai [a], Ying Li [a], Yifan Luo [a,b], Marc Debliquy [b], Chao Zhang [a,*]

[a] College of Mechanical Engineering, Yangzhou University, Yangzhou 225127, PR China
[b] Service de Science des Matériaux, Faculté Polytechnique, Université de Mons, Mons 7000, Belgium

ARTICLE INFO

Keywords:
Gas sensors
Exhaled breath detection
Lung cancer
Lanthanum ferrite
Isopropanol

ABSTRACT

The early detection of lung cancer by breath analysis has attracted more and more attention. In this work, high-performance $LnFeO_3$ (Ln = Nd, Dy, Er) based isopropanol sensors were synthesized by microwave-assisted hydrothermal method. X-ray diffraction, field-emission scanning electron microscope, transmission electron microscope, and UV–visible-near infrared absorption spectrometer were used to analyze the material phase composition, microstructure, and other physical properties. The sensing performance was tested by using a four-channel gas testing chamber. The sensors were tested with low concentrations of isopropanol at high humidity to simulate a real human exhaled breath environment. The low binding energy of the Ln-O bond makes it easy to have chemical reactions, which leads to excellent isopropanol sensing performance. Finally, the gas sensing mechanism of the $LnFeO_3$ sensor was discussed.

1. Introduction

Cancer has become a major killer which threatens human health and has brought a significant burden to society, attracting widespread attention. In 2022, there could be 20.2 million new cancer cases worldwide [1]. The number of people dead of cancers is 14 million per year, 11 percent of which are lung cancer [2]. Treating lung cancer is a long and challenging process, and the survival time of patients is generally less than five years. In the early stage of lung cancer, timely detection and corresponding treatment can significantly improve the survival rate. However, the symptoms of early-stage lung cancer are not evident, including shortness of breath, coughing, and weight loss, which are similar to pneumonia or tuberculosis. As a result, efficient lung cancer detection methods are urgently needed.

The commonly used detection methods for early lung cancer diagnosis include medical imaging, cytological and histopathological examination, and tumor marker detection. However, they all have limitations, such as high cost and poor detection sensitivity. Computed Tomography (CT), one of the most important methods to detect cancer, also increases the risk of cancer due to radiation exposure [3]. Biopsy techniques are also commonly used, but are expensive and highly experienced [4]. Therefore, a cheap and efficient test is urgently needed. Respiratory is one of the most popular detection methods in recent years due to its flexibility, user-friendly and low cost. The volatile organic compounds (VOCs) can be found in human exhaled breath and their concentrations vary with the health condition [5]. The sensor technology can be used to detect potential lung cancer by monitoring changes in the composition and concentration of VOCs contained in exhaled breath [6]. According to a literature review, concentrations of certain VOCs exhaled by lung cancer patients are different from those exhaled by ordinary patients, and these gases are considered as biomarkers for lung cancer. Among those VOCs, EtOH [7], propanone [8], normal butanol [9], methanol [10] and isopropanol are determined as typical biomarkers [11]. For the detection of these biomarkers, Gas Chromatography-Mass Spectrometry (GC–MS) technology is an effective method [12]. However, it is limited in practicality as an initial screening method due to high price, heavy equipment and high technical requirements.

Metal oxide sensor has high sensitivity and low cost, acting as a suitable sensor for testing VOCs in low concentration [13-16]. Typical metal oxides have been widely used in detecting VOCs , e.g. ZnO [17], SnO_2 [18], In_2O_3 [19]. However, these metal oxides have some limitations, such as high working temperature and poor stability [20]. Perovskite-type ABO_3 oxides have thermal stability and rapid oxygen

* Corresponding author.
E-mail address: zhangc@yzu.edu.cn (C. Zhang).

https://doi.org/10.1016/j.apsusc.2022.154292
Received 7 June 2022; Received in revised form 8 July 2022; Accepted 14 July 2022
Available online 16 July 2022

mobility [21,22]. It is suitable as a sensing material for gas detection of VOCs. Zhang et al. confirmed that zinc ferrite could be used to test 1 ppm of acetone [23,24]. In these sensing materials, $LnFeO_3$ (Ln stands for lanthanide) with perovskite structure shows excellent potential in detecting VOCs gas [25-27]. Siemons et al. found that the Ln-O bond was the key factor which affected the sensors [28]. This prompted people to prepare $LnFeO_3$ materials to detect VOCs.

In this paper, isopropanol was selected as the target gas. It is important to prepare an isopropanol sensor with high sensitivity, humidity resistance and stability [29]. $LnFeO_3$-based sensing materials would be a good choice. So far, $DyFeO_3$, $ErFeO_3$ and $NdFeO_3$ have been proved to have good detection ability of volatile organic gases, especially for acetone, isopropanol and ethanol [30-32] for their unique magnetic, chemical stability and photocatalytic applications [33-35]. It means $LnFeO_3$(Ln = Nd, Dy, Er) may be a good isopropanol gas detection material. However, the basic preparation methods of $LnFeO_3$(Ln = Nd, Dy, Er) were hydrothermal method and sol–gel method. These methods usually take a long time which may make the material subjected to a temperature gradient during heating. The microwave-assisted hydrothermal method is a fast, simple, and uniform method for the preparation of sensing materials [36]. For example, in the study of rGO-ZnO by Meti et al., they adopted microwave hydrothermal method and completed the synthesis in only 10 min under the microwave hydrothermal method with a radiation frequency of 2.45 GHz and power of 700 W [37]. In Kavitha et al. 's study, the ordinary hydrothermal method process required seven hours of heating [38]. In the synthesis of SnO_2, the ordinary hydrothermal method adopted by Xu et al. required 12 h of heat preservation when heated to 160 ℃[39]. However, the microwave hydrothermal method studied by Man et al. could complete the reaction by keeping it at 160 ℃ for 30 min [40]. Due to the strong penetration performance of microwave, which is enough to input high energy into the material, the internal temperature of the material is increased quickly. The microwave-assisted hydrothermal method has great potential in industrial applications, because the heating process is less affected by temperature gradient [41]. As mentioned above, $LnFeO_3$(Ln = Nd, Dy, Er) has rarely been mentioned as a gas sensing material for detecting isopropanol, especially prepared by microwave hydrothermal synthesis [42].

For the first time, $LnFeO_3$(Ln = Nd, Dy, Er) synthesized by the microwave-assisted hydrothermal method was used as a sensing material to detect isopropanol. The effects of Nd, Dy and Er elements on gas sensing performance were studied, and the mechanism was discussed.

2. Material and methods.

2.1. Chemicals

The chemical raw materials used in this experiment were all purchased from Shanghai (Aladdin Biochemical Technology Co., Ltd.) without further purification, including iron (III) nitrate nonahydrate ($Fe(NO_3)_3{\cdot}9H_2O$), neodymium nitrate ($Nd(NO_3)_3{\cdot}6H_2O$), dysprosium nitrate ($Dy(NO_3)_3{\cdot}6H_2O$), erbium nitrate ($Er(NO_3)_3{\cdot}6H_2O$), cetyltrimethylammonium bromide (CTAB), ammonia and ethanol.

2.2. Synthesis of $LnFeO_3$

55 mL ethanol-deionized water (DW) mixture was prepared (volume ratio of EtOH to DW was 38:17). 2 mmol $Fe(NO_3)_3{\cdot}9H_2O$ was dissolved into the mixture. 2 mmol $Nd(NO_3)_3{\cdot}6H_2O$, $Dy(NO_3)_3{\cdot}6H_2O$, and $Er(NO_3)_3{\cdot}6H_2O$ were added into the solution separately after the $Fe(NO_3)_3{\cdot}9H_2O$ stirred to dissolve. The mixture was kept stirring until the solids dissolved to obtain a colored transparent solution. After that, 1166 mg CTAB was added to the solution and stirred for 10 min. Ammonia was used to adjust the pH value, and the pH value of the mixture was adjusted to 9. The solution was transferred into a 100 mL Teflon-lined autoclave for the microwave-assisted hydrothermal step. The microwave power was set as 500 W and the heating rate was 5 °C / min. The reactor was placed in a microwave hydrothermal synthesizer for 30 min at 170 °C. After cooling naturally, the powders were washed with DW three times and centrifuged. After drying at 80 °C for 10 h, the resulting solids were ground into powders, placed in a crucible and heat-treated at 800 °C for 2 h in a muffle furnace to remove organic impurities. The heating rate was 10 °C / min.

2.3. Characterization

The phase structure of $LnFeO_3$ was analyzed by X-ray diffraction (XRD, D8 Advance Bruker), and $CuK_{\alpha 1}$ radiation was chosen as the X-ray source. The scanning range of 2θ was from 10° to 80°. The morphologies were observed by a field-emission scanning electron microscope (FE-SEM, S4800 Hitachi) and transmission electron microscope (TEM, JEM-2100). The quantity and chemical valence of elements and the oxygen defects in $LnFeO_3$ were characterized by an X-ray photoelectron spectrometer (XPS, ESCALAB 250Xi). UV–visible-near infrared absorption spectrometer (Cary 5000) was used to measure the ultraviolet and visible absorption spectrum of $LnFeO_3$. The specific surface area of $LnFeO_3$ was measured using Brunauer-Emmett-Teller (BET) method.

2.4. Preparation of sensing materials

The tests were carried out in a homemade testing system, as exhibited in Fig. 1. The testing system adopts a four-channel testing chamber. Pure synthetic air was purchased from Yangzhou Ruite Gas company limited. Four mass flowmeters (El-flow, Bronkhorst) were purchased from Beijing Artim Control Equipment company. The Pt/Au electrodes coated on Al_2O_3 were purchased from Wuhan Huachuang Ruike Technology company limited and used as the sensor substrates. During testing, two independent flowmeters were used to control the inflow of wet and dry air to adjust relative humidity. The VOCs were generated by dropping quantitative VOCs liquid into DW according to Henry's law. The sensor response (S) was defined as the ratio of the resistance of $LnFeO_3$ in target gas (R_g) and air (R_a), namely $S = R_g/R_a$. Response/recovery time is defined as the time required to reach 90% of the maximum response/recovery to the baseline. A small amount of the above $LnFeO_3$ powder was mixed with water to prepare a suspension and then coated on the Pt electrode. After drying naturally, it was put into the oven at 120 °C for 10 h.

3. Results and discussion

3.1. Material characterization

To analyze the phase structure of the $LnFeO_3$, XRD analysis was performed. The XRD patterns of the three samples are displayed in Fig. 2 (a)-2(c). Peaks of $NdFeO_3$ are located at 22.7°, 25.4°, 32.4°, 46.5°, 58.4°, and 68.1°, corresponding to the faces of (110), (111), (112), (220), (312), (224) respectively which fit well with orthorhombic $NdFeO_3$ (JCPDS, 74–1473). Peaks of $DyFeO_3$ are located at 23.0°, 25.8°, 32.9°, 33.7°, 53.4°, and 59.1°, which are respectively corresponding to the faces of (110), (111), (112), (200), (131), (312). All the peaks fit well with orthorhombic $DyFeO_3$ (JCPDS, 74–1478). In Fig. 2(c), peaks of $ErFeO_3$ are located at 23.2°, 25.9°, 33.2°, 33.9°, 53.5°, and 60.3°, which correspond to the faces of (110), (111), (112), (200), (301), and (312) respectively. All the main peaks fit well with orthorhombic $ErFeO_3$ (JCPDS, 74–1480).

The morphology of the prepared $LnFeO_3$ powder was observed, as exhibited in Fig. 2 (e)-2(f). Generally speaking, $LnFeO_3$ exhibits a nanoparticle shape and the particle size is 70–100 nm. After high-temperature heat treatment, the particles were stacked and agglomerated. TEM was used to observe the particles, as shown in Fig. 3. The same phenomenon was observed by TEM, and the agglomeration of nanoparticles was also observed. It is speculated that the sintering may

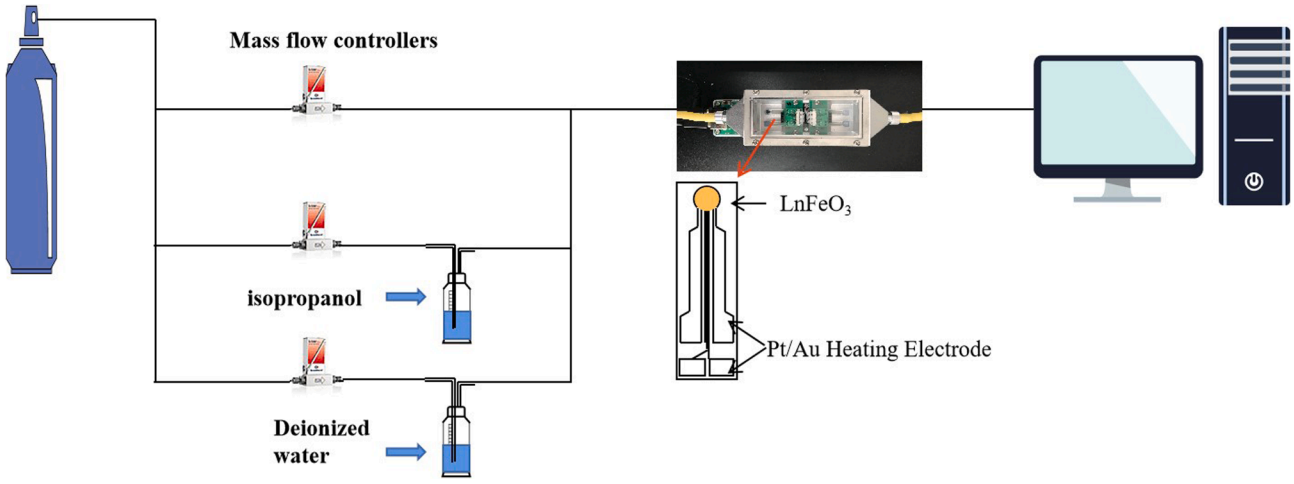

Fig. 1. Schematic of the gas sensing setup.

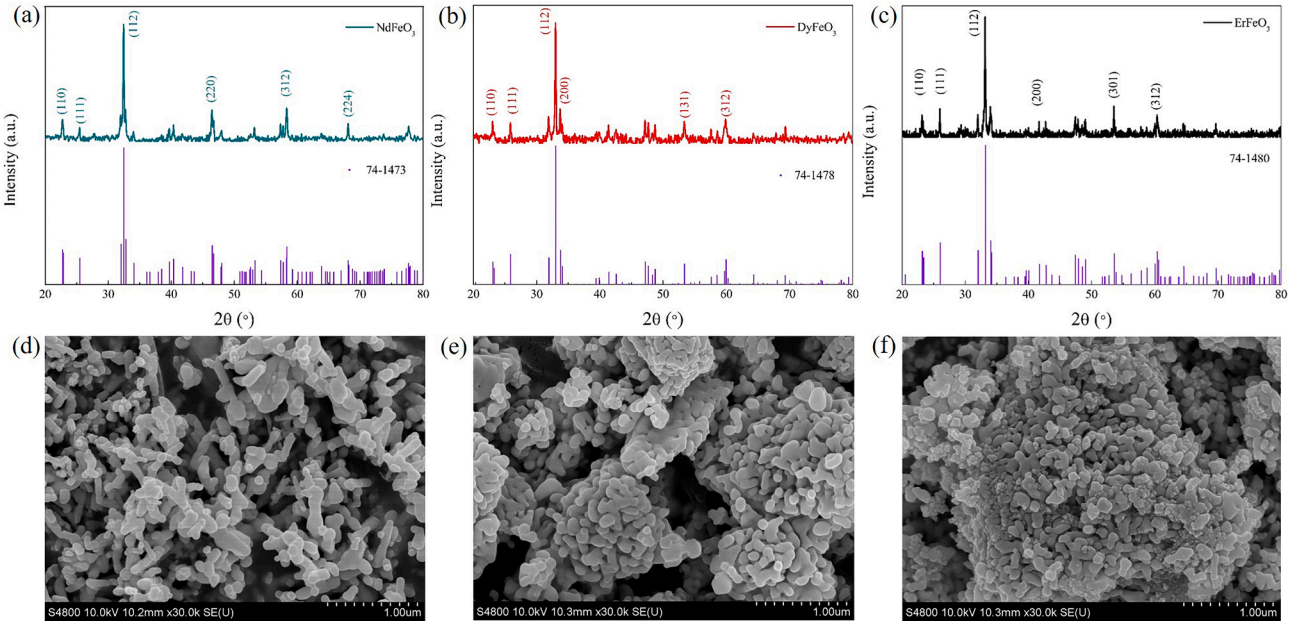

Fig. 2. X-ray diffraction patterns of $LnFeO_3$: (a)$NdFeO_3$; (b)$DyFeO_3$; (c) $ErFeO_3$; and SEM image of $LnFeO_3$: (d)$NdFeO_3$; (e)$DyFeO_3$; (f) $ErFeO_3$.

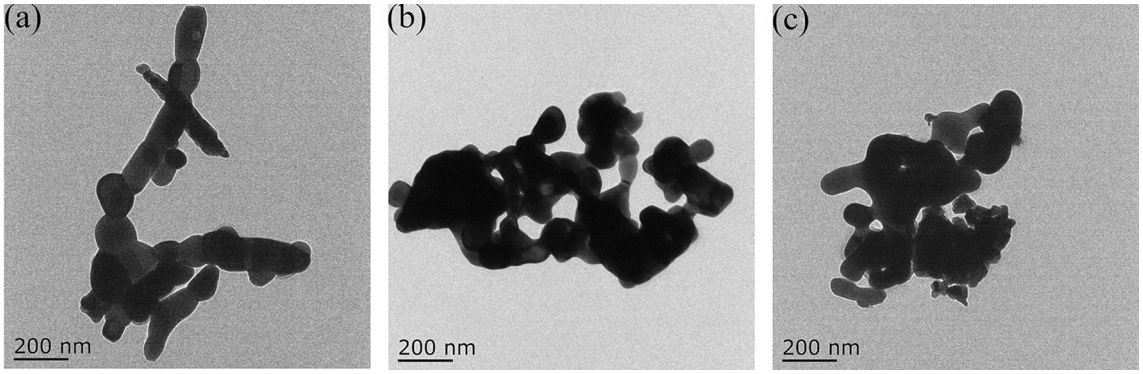

Fig. 3. TEM images of $LnFeO_3$: (a)$NdFeO_3$; (b)$DyFeO_3$; (c)$ErFeO_3$.

be ascribed to high calcination temperature.

To study the chemical states of $LnFeO_3$ surface elements, XPS was used. As shown in Fig. 4(a) and 4(e), the elements of $LnFeO_3$ materials include Nd, Dy, Er, Fe, O, and C, among which the C1s peak located at 284.8 eV from the contamination was used as the reference for energy calibration in the test. The peak positions of Fe 2p are 724.12 eV and

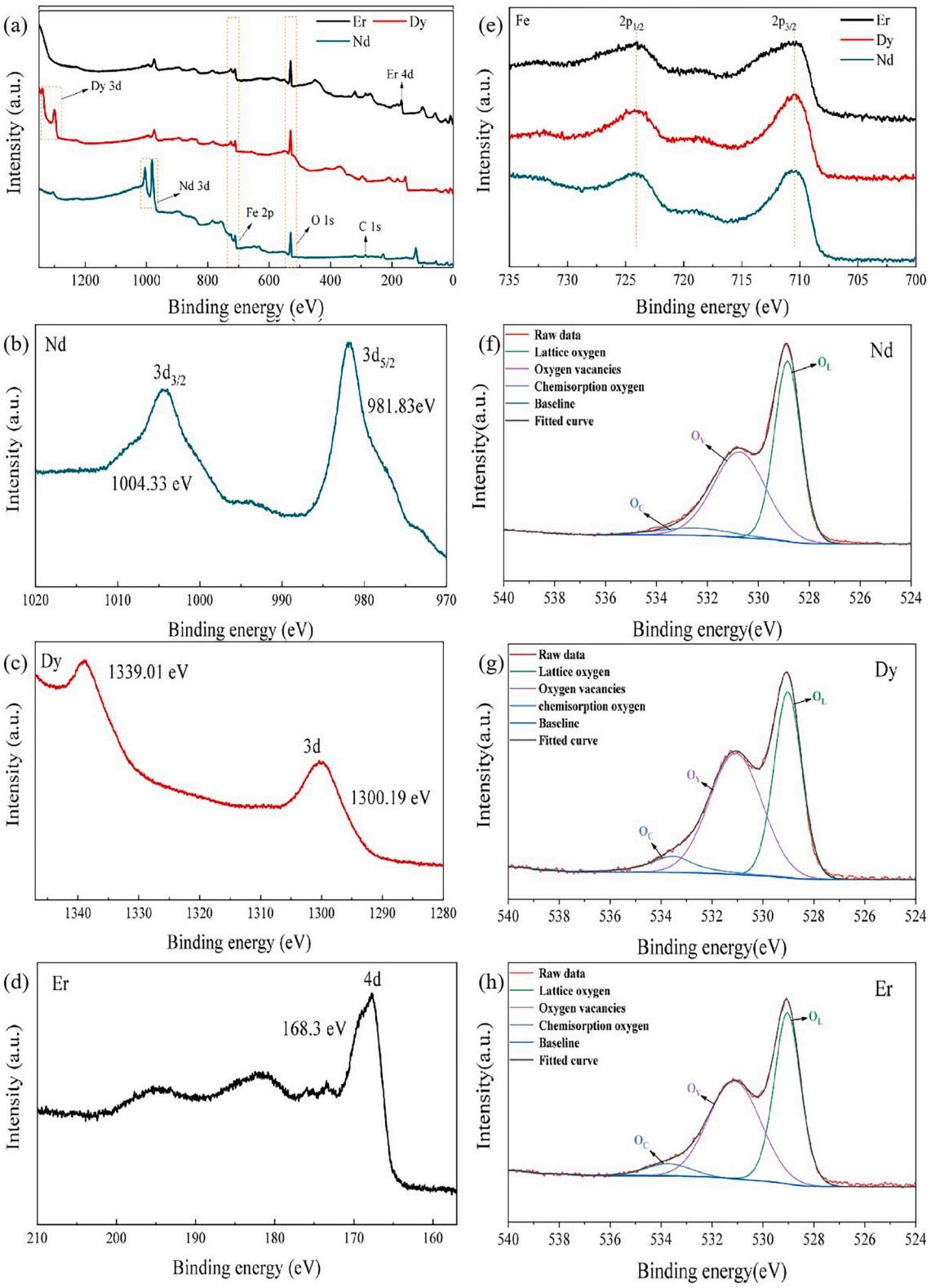

Fig. 4. (a) XPS full survey spectra of $LnFeO_3$; high resolution XPS spectra of (b)Nd3d, (c) Dy3d, (d) Er4d, (e) Fe2p; high resolution XPS spectra of O1s: (f) $NdFeO_3$, (g) $DyFeO_3$, (h) $ErFeO_3$.

710.45 eV, corresponding to $2p_{1/2}$ and $2p_{3/2}$, indicating that Fe^{3+} existed [43]. From a high-resolution XPS analysis of each element, it could be seen that the Er 4d spectrum consists of a wide peak located at approximately 168.3 eV, suggesting there existed Er^{3+} [44]. The Nd 3d spectrum consists of wide peaks at 1004.33 eV and 981.83 eV, indicating the presence of Nd^{3+}. The Dy 3d spectrum is composed of wide peaks at 1339.01 eV and 1300.19 eV, indicating the existence of Dy^{3+}. As depicted in Fig. 4(b-d), during the annealing process, the atoms are rearranged, resulting in the formation of crystals. The weakly bonded oxygen atoms move away from their original positions, creating oxygen

defects. As shown in Fig. 4(f-h), from high-resolution XPS spectrum of O1s, it could be found that the spectrum of O1s can be split into three peaks. As shown in Fig. 4(f), the peak located at 529.78 eV corresponds to lattice oxygen (O_L).The middle peak located at 531.71 eV is related to oxygen vacancies (O_V). The last peak of 532.73 eV corresponds to chemisorption oxygen (O_C) [32]. As shown in Fig. 4(g), the first peak of 529.0 eV corresponds to lattice oxygen (O_L). The second peak of 531.0 eV is related to oxygen vacancies (O_V). The last peak of 533.5 eV corresponds to chemisorption oxygen (O_C) [30]. As shown in Fig. 4 (h), the lattice oxygen (O_L), the oxygen vacancies (O_V) and the chemisorption oxygen (O_C) were related to the peak position approximately at 529.9 eV , 531.5 eV , 533.3 eV [31]. In gas reactions, the oxygen molecules tend to adsorb on the sites of oxygen vacancies and generate oxygen ions. At the same time, reduction reactions tend to occur at ion sites and oxygen deficiency sites [23]. This was consistent with the previous research results of gas reactions on the surface of perovskite metal oxide sensor materials [45]. In conclusion, the presence of oxygen defect was observed on the surface of $LnFeO_3$ material, proving the possibility of an effective reaction between reducing gas and oxygen defect.

Fig. 5(a)-5(c) are nitrogen adsorption/desorption curves of $LnFeO_3$. According to the samples' isotherm and average pore size analysis, $LnFeO_3$ had high porosity, as shown in Table 1. The BET of $NdFeO_3$, $DyFeO_3$ and $ErFeO_3$ were 8.142, 9.679 and 9.800 $m^2 \cdot g^{-1}$, respectively.

The UV–Visible absorption spectrum of $LnFeO_3$ (Ln = Dy, Nd, Er) was shown in Fig. 5(e-f). It could be seen that within the scope of 200–800 nm, the spectrum had a wide absorption band, and the narrow bandgap width of $LnFeO_3$ nanoparticles may lead to this situation. According to the Kubelka-Munk theory [46], the bandgap energy of the material was calculated. The bandgap energies of $NdFeO_3$, $DyFeO_3$, $ErFeO_3$ were 2.18 eV, 2.05 eV and 1.96 eV. The width of the bandgap is inversely proportional to the difficulty of electron transition. When the bandgap is narrow, electrons in valence band are easier to be excited to transfer to conduction band, which means the activity of the material getting better [47].

3.2. Gas sensing performance

The effective VOC component concentration in exhaled air detection is low, usually at the ppb level. The difference between patients and healthy people is quite small, so the response of the sensors needs to be high enough to show the difference. Therefore, it was important to measure the gas sensitivity of low concentration isopropanol. The gas sensing test of 2 ppm isopropanol was carried out at a humidity of 50%, as shown in Fig. 6(a)-6(b). The three materials showed the best gas sensitivity response at 275 °C. Therefore, 275 °C was selected as the optimal working temperature for isopropanol. Fig. 6(c)-6(d) showed that $LnFeO_3$ material had an excellent response to 0.2–2 ppm isopropanol at the optimal operating temperature. Even for 0.2 ppm isopropanol, the sensor showed a clear response curve. Although $NdFeO_3$ had a small specific surface area, its sensitivity may be higher than that of $DyFeO_3$ and $ErFeO_3$ due to its high oxygen defect concentration ($NdFeO_3$, $DyFeO_3$, Er FeO_3 O_V:56.4%, 54.1%%, 54.7%).

The VOCs in the exhaled breath have not only low concentration, but also high humidity. Water molecules have competitive adsorption with the oxygen ions on the surface, thus affecting the gas sensing performance. To study the effect of humidity on the sensing performance of $LnFeO_3$ material, the gas sensitivity test of 1 ppm isopropanol was carried out at 275 °C under different relative humidity. As exhibited in Fig. 7(a)-7(b), the baseline resistance of $LnFeO_3$ material increased with the growth of humidity, and the response value also changed. $ErFeO_3$ showed a clear rule that the response decreased with humidity growth. $DyFeO_3$ and $NdFeO_3$'s response showed a slight increase trend with the increase of humidity and finally reduced with the increase of humidity, which demonstrates good humidity resistance, providing a premise for $LnFeO_3$ detection of respiratory gas. Fig. 7(c)-7(d) indicated that LnFeO3 material still had an excellent response to isopropanol at low concentrations, even under high humidity. When the material was exposed to 0.2 ppm isopropanol, the resistance changes showed a clear response with a high signal-to-noise ratio. The response could reach

Table 1
Textural properties obtained from N_2 isotherm.

Name	Specific surface area/ $m^2 \cdot g^{-1}$	Average pore diameter/nm	Pore volume/ $cm^3 \cdot g^{-1}$
$NdFeO_3$	8.142	2.967	0.038
$DyFeO_3$	9.679	3.314	0.069
$ErFeO_3$	9.800	11.972	0.087

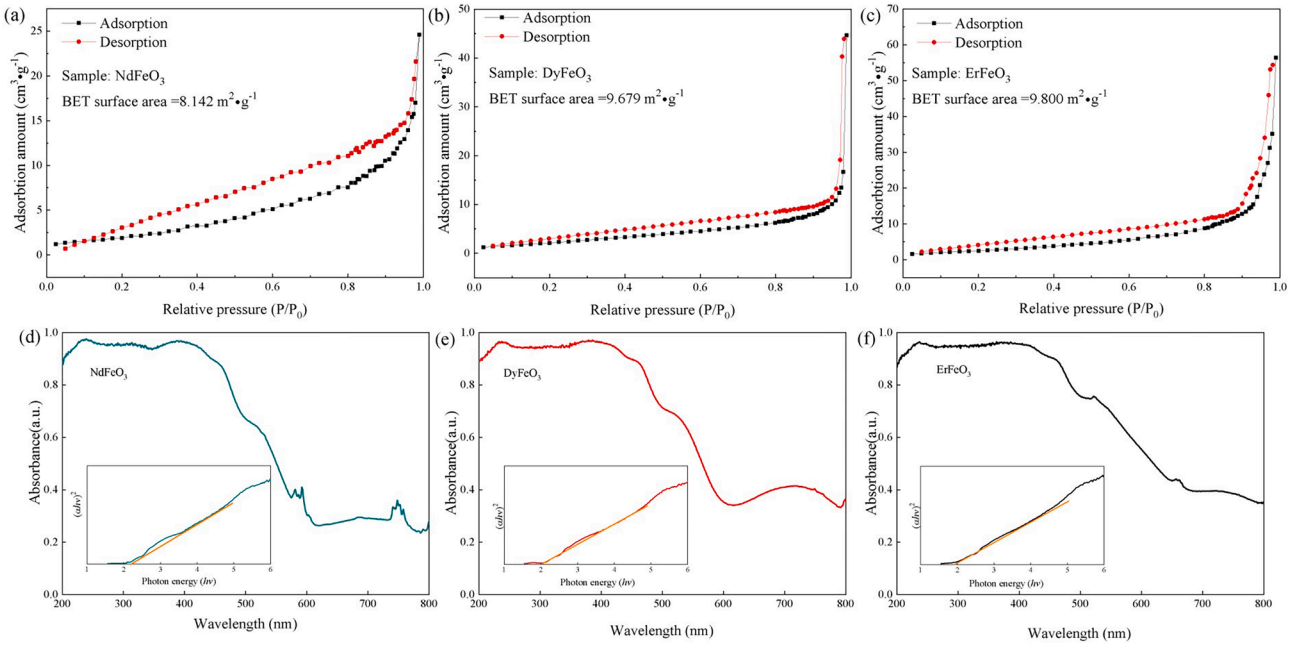

Fig. 5. Nitrogen adsorption desorption isotherm of $LnFeO_3$ materials: (a) $NdFeO_3$, (b) $DyFeO_3$, (c)$ErFeO_3$ and ultraviolet visible absorption spectrum of $LnFeO_3$ samples: (d) $NdFeO_3$, (e) $DyFeO_3$, (f)$ErFeO_3$. The inserts are the calculated bandgaps.

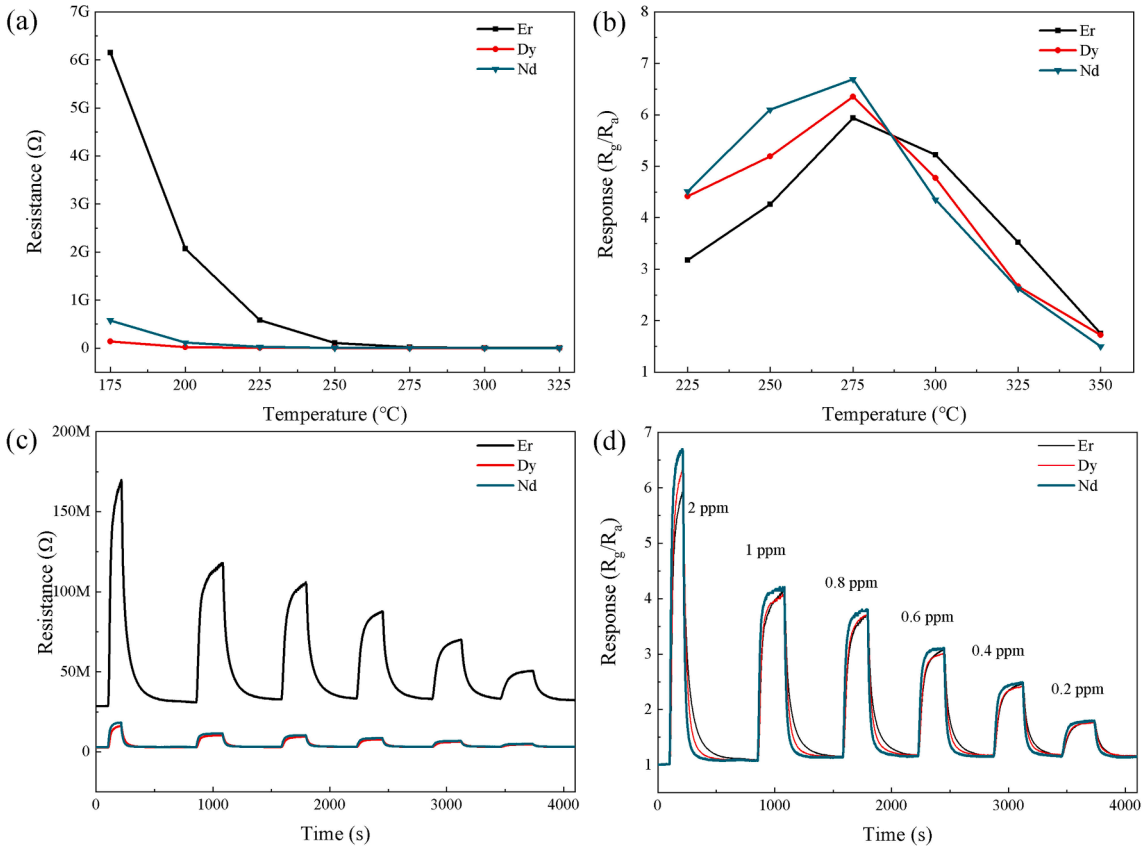

Fig. 6. (a) Curves of resistance value of $LnFeO_3$ material with temperature, (b) gas sensing response of $LnFeO_3$ material to 2 ppm isopropanol at 225–350 °C, (c) response resistance curve of $LnFeO_3$ material to 0.2–2 ppm isopropanol at 275 °C, (d) response curve of $LnFeO_3$ material to 0.2–2 ppm isopropanol at 275 °C (50% relative humidity).

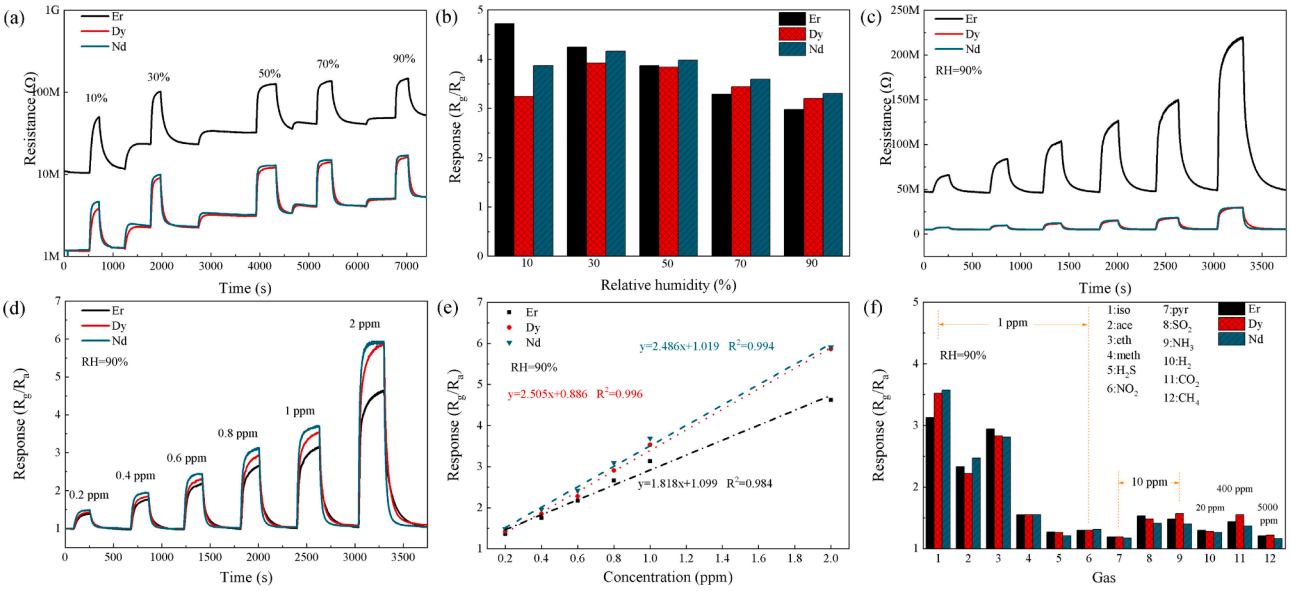

Fig. 7. Resistance curve of response to 1 ppm isopropanol at 275 °C (a) 10–90% relative humidity, (b) change of response value of $LnFeO_3$ material to 1 ppm isopropanol with humidity; responses of $LnFeO_3$ material to ultra-low concentration isopropanol at 275 °C and 90% relative humidity (c) resistance change curve, (d) response curve.(e) response concentration linear fitting curve of $LnFeO_3$ material to low concentration isopropanol, (f) selectivity of $LnFeO_3$ materials (including isopropanol, acetone, ethanol, methanol, pyridine).

around 1.5.

Fig. 7 (e) showed the relationship between $LnFeO_3$ response and target gas concentration. Its response exhibited an excellent linear relation with the gas. Among them, the response-concentration linear fitting correlation coefficients of the three materials were all greater than 98%, among which $DyFeO_3$ was the highest (99.6%) with the

highest degree of coincidence. The challenges for exhaled breath detection lie in small changes in the target gas concentration and the complicated gas composition. Good selectivity is one of the important parameters of gas sensing materials. We conducted the following experiments to test its selectivity: under the optimal working temperature and 90% relative humidity, the sensor responses to 12 different gases were tested, as shown in Fig. 7 (f). In addition to a good response to isopropanol, $LnFeO_3$ also showed an excellent response to acetone and ethanol, but a poor response to H_2S, NO_2, SO_2 and other gases.

In the process of gas reaction, the response/recovery rate of the material is also important for gas sensing performance. All three kinds of sensors can respond quickly to a low concentration of gas. As exhibited in Fig. 8(a)-8(b), the response process of 1 ppm isopropanol was analyzed at 90% relative humidity and the optimal working temperature to simulate the working condition with exhaled breath. It was found that $LnFeO_3$ material had a fast response/recovery speed. The response times of the three materials to 1 ppm isopropanol were 109 s, 98 s, and 57 s, respectively. The recovery times of the three materials are 141 s, 95 s, and 52 s, respectively, among which $NdFeO_3$ had the fastest recovery rate and $ErFeO_3$ had the lowest recovery rate.

Fig. 8(d)-8(e) showed the response cycle of $LnFeO_3$ material to 1 ppm isopropanol. Both the resistance and response curve showed good repeatability, and the resistance can recover well after testing.

To study the long-term stability of the $LnFeO_3$ sensor, the sensor is tested with 1 ppm isopropanol at 275 °C and 90% relative humidity once per day for over 30 days, and its response was recorded, as shown in Fig. 8(f). A total of 15 tests were conducted over 30 days. $LnFeO_3$ sensor showed good stability, and the response did not vary sharply, maintaining a good response. Table 2 shows the parameters commonly used to test isopropanol for metal oxides. Under the condition that humidity greatly influences the detection response of isopropanol, the synthesis scheme provided in this paper still has a better response than most materials in dry air.

3.3. Gas sensing mechanism

The sensing mechanism of $LnFeO_3$ sensor is generally clarified based on the adsorption and desorption of target gas on the material surface, leading to the electron transfer between the gas molecule and the surface. Taking $NdFeO_3$ as an example, Fig. 9 shows the gas mechanism of $LnFeO_3$. When the sensor is in air, a large number of oxygen molecules in the atmosphere are adsorbed on the material surface [60], and electrons are captured to form oxygen ions ($O^{2-}_{(ad)}$, $O^{-}_{(ad)}$), which increase the number of holes in the material conduction. A hole accumulation layer will form close to the surface and increase conductivity since the $NdFeO_3$ is a p-type semiconductor, and the energy band will bend to the higher energy side, as shown in Formulas (1) and (2) [61]. When the test chamber is permeated with isopropanol, isopropanol molecules react with oxygen ions adsorbed on the material surface, producing CO_2 and H_2O and releasing electrons simultaneously, as shown in Formulas (3–4) [30]. Electrons return to the conduction band of the material, resulting in a decrease in the number of holes in the conduction band, which reduces the conductivity, so the resistance increases [62,63].

$$O_{2\ (ad)} + 2e^- \rightarrow 2O^-_{(ad)} \quad (1)$$

$$O_{2\ (ad)} + 4e^- \rightarrow 2O^{2-}_{(ad)} \quad (2)$$

$$CH_3CHOHCH_3\ (ad) + 9O^-\ (ad) \rightarrow 3CO_2 + 4H_2O + 9e^- \quad (3)$$

$$CH_3CHOHCH_3\ (ad) + 9O^{2-}\ (ad) \rightarrow 3CO_2 + 4H_2O + 18e^- \quad (4)$$

On the other side, the excellent response is due to the binding energy of the Ln-O bond [28]. From the overall trend analysis, the absolute value of Ln-O bond binding energy is inversely proportional to the gas sensing response of the material. Lower binding energy leads to an easily broken Ln-O bond, and it is easy to generate atomic vacancies in its crystal structure. The increase in surface defects causes more reactive oxygen species to adsorb on the material surface and speeds up the electron transfer [28,54]. When the material is in target gas, such as isopropanol, oxygen ions react chemically with target gases such as isopropanol and release electrons, which accelerates the gas reaction. The formula of calculating Ln-O is [28]:

$$\Delta H(Ln-O) = \frac{1}{CN}\left(H_f - H_s \cdot m - \frac{n}{2}Do\right) \quad (5)$$

H_f is the energy required to generate M_mO_n oxide per mole, H_s is the sublimation energy of each metal, Do is the dissociation energy of O_2, CN is the coordination number of metal ions. The absolute value relation of the L-O bond binding energy of several materials involved is Er-O > Nd-

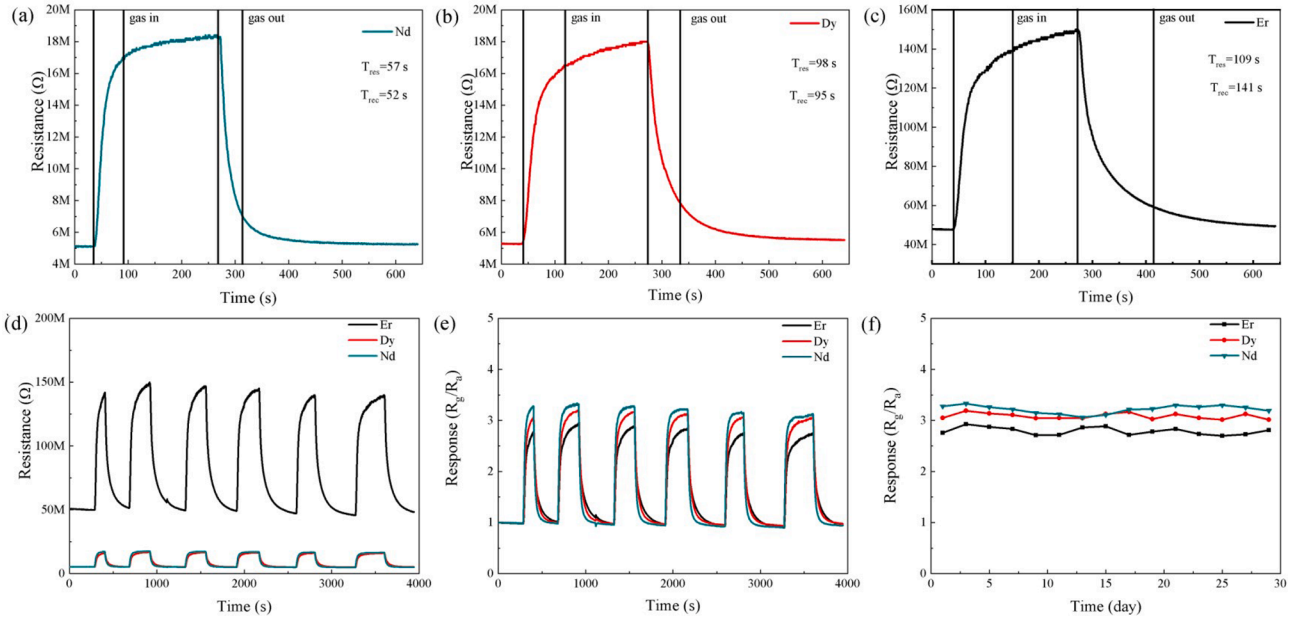

Fig. 8. Response recovery curves of $LnFeO_3$ material to 1 ppm isopropanol at 275 °C and 90% relative humidity: (a) $NdFeO_3$, (b) $DyFeO_3$, (c) $ErFeO_3$; six response cycles to 1 ppm isopropanol at 275 °C and 90% relative humidity, (d) resistance variation curve, (e) response curve; (f) response value curve of $LnFeO_3$ sensors to 1 ppm isopropanol within 30 days.

Table 2
Comparison of different metal oxide-based isopropanol sensors.

Sensing materials	Detection concentration	Operating temperature	Response	Relative humidity	Synthetic methods	Refs.
$BiFeO_3$	2 ppm	240 °C	4.8[1]	0 %	Sol-gel method	[48]
SnO_2 nanorods	100 ppm	325 °C	12[2]	0%	Chemical precipitation	[49]
CdS/ZnO	10 ppm	320 °C	6.97[1]	0%	Wet-chemical method	[50]
$ZnMn_2O_4$	100 ppm	250 °C	78 %[3]	60%	Sol-gel method	[51]
SnO_2 nanorods	100 ppm	255 °C	4.7[2]	0%	Chemical precipitation	[52]
g-C_3N_4/SnO_2	1 ppm	200 °C	4.61[2]	0%	Hydrothermal method	[24]
Gd-SnO_2	300 ppm	300 °C	14[2]	0%	Straightforward co-precipitation method	[53]
Ag-In_2O_3	1 ppm	300 °C	3.2[2]	0%	Hydrothermal method	[54]
$ErFeO_3$	100 ppm	270 °C	1.2[1]	90%	Hydrothermal method	[55]
MoO_3/TiO_2/$Ti_3C_2T_x$ nanocomposite	50 ppm	Room temperature	53.7 %[4]	<60%	Etching	[56]
Au@ZnO Nanofilms	1 ppm	300 °C	7[1]	0%	Magnetron Sputtering	[57]
NiO/CeO_2 nanocomposites	5 ppm	Room temperature	75[2]	0%	Coprecipitation method	[58]
CuO/SnO_2	100 ppm	280 °C	50.4[1]	0%	Hydrothermal method	[59]
$NdFeO_3$	0.8 ppm	275 °C	3.81[1]	90 %	Microwave hydrothermal method	This work
$DyFeO_3$	0.8 ppm	275 °C	3.73[1]	90 %	Microwave hydrothermal method	This work
$ErFeO_3$	0.8 ppm	275 °C	3.72[1]	90 %	Microwave hydrothermal method	This work

1:S = R_g/R_a, 2:S = R_a/R_g, 3: S=(R_a-R_g)/R_a × 100%, 4: S=(R_g-R_a)/R_a × 100%

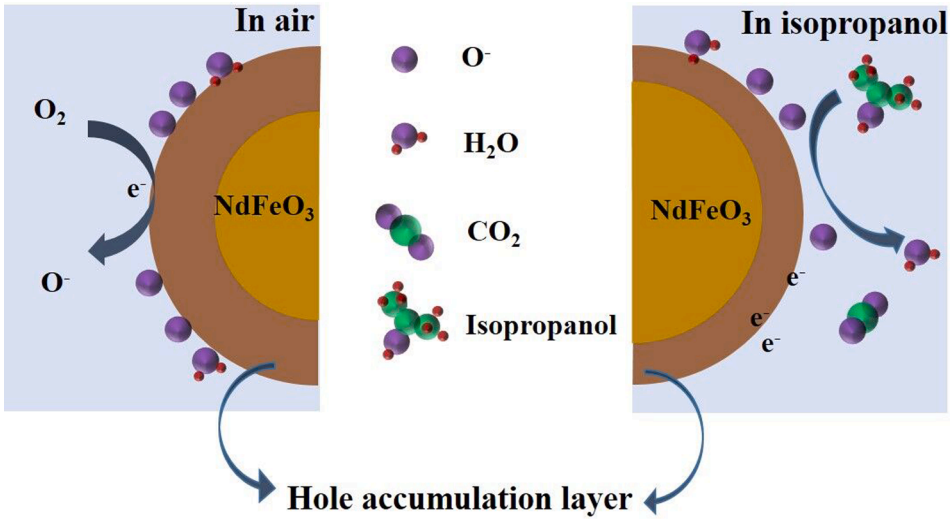

Fig. 9. Sensing mechanism diagrams of $NdFeO_3$ sensor.

O > Dy-O [25]. Theoretically, $DyFeO_3$ is the excellent gas sensing properties of the three materials. The absolute value difference between Nd-O bond and Dy-O bond is slight, so there is little difference in their gas sensitivity. In addition, the sensitivity of $NdFeO_3$ to isopropanol in this paper was slightly stronger than that of $DyFeO_3$. The performance of the three materials conformed to the theoretical analysis. At the same time, BET of the material can also affect the gas sensing properties by affecting the gas adsorption process. The specific surface area is proportional to the reaction sites provided to the gas. When the rate of electron exchange between the material surface and adsorbed gas increases, the gas sensing performance will be improved [64].

4. Conclusion

Three $LnFeO_3$ (Ln = Nd, Dy, Er) perovskite structured materials were synthesized using a microwave-assisted hydrothermal method. The material microstructure was characterized, and its properties were tested to study why the $LnFeO_3$ ternary oxide of La element had an excellent response to isopropanol. The excellent gas-sensing performance of $LnFeO_3$ is owing to the low Ln-O bond energy of Ln series elements, which is easy to break and react with oxygen ions [65]. Meanwhile, the gas sensing performance of $LnFeO_3$ is also affected by specific surface areas. The $LnFeO_3$ material had excellent sensing performance to isopropanol and could detect isopropanol lower than 0.2 ppm at 275 °C. The $LnFeO_3$ materials also showed good humidity resistance and selectivity. The $LnFeO_3$ material showed a promising potential for the applications of exhaled breath detection.

CRediT authorship contribution statement

Hongfeng Chai: Investigation, Writing – original draft. **Ying Li:** Investigation, Writing – original draft. **Yifan Luo:** Writing – review & editing. **Marc Debliquy:** Writing – review & editing. **Chao Zhang:** Conceptualization, Supervision, Funding acquisition, Resources, Writing – review & editing.

Declaration of Competing Interest

The authors declare that they have no known competing financial interests or personal relationships that could have appeared to influence the work reported in this paper.

Acknowledgments

This work is supported by the Outstanding Youth Foundation of Jiangsu Province of China under Grant No. BK20211548, the National Natural Science Foundation of China under Grant No. 51872254 and the National Key Research and Development Program of China under Grant No. 2017YFE0115900.

References

[1] R.L. Siegel, K.D. Miller, H.E. Fuchs, A. Jemal, Cancer Statistics, CA Cancer J. Clin. 71 (2021) 7–33, https://doi.org/10.3322/caac.21654.
[2] Q. Sun, C. Peng, B. Cong, Y. Hao, J. Guo, Y. Zhao, X. Zhao, Involvement of syk and VEGF-C in invasion of lung adenocarcinoma A549 cells, J. Cancer Res. Ther. 12 (2016) 640–644, https://doi.org/10.4103/0973-1482.150413.
[3] N. Journy, J.L. Rehel, H. Ducou Le Pointe, C. Lee, H. Brisse, J.F. Chateil, S. Caer-Lorho, D. Laurier, M.O. Bernier, Are the studies on cancer risk from CT scans biased by indication? Elements of answer from a large-scale cohort study in France, Brit. J. Cancer. 112 (2015) 185–193, https://doi.org/10.1038/bjc.2014.526.
[4] N. Ishibashi, T. Maebayashi, T. Aizawa, M. Sakaguchi, M. Okada, Serum tumor marker levels at the development of intracranial metastasis in patients with lung or breast cancer, J Thorac Dis. 11 (2019) 1765–1771, https://doi.org/10.21037/jtd.2019.05.37.
[5] H. Haick, Y.Y. Broza, P. Mochalski, V. Ruzsanyi, A. Amann, Assessment, origin, and implementation of breath volatile cancer markers, Chem. Soc. Rev. 43 (2014) 1423–1449, https://doi.org/10.1039/C3CS60329F.
[6] W. Ma, P. Gao, J. Fan, Y. Hashi, Z. Chen, Determination of breath gas composition of lung cancer patients using gas chromatography/mass spectrometry with monolithic material sorptive extraction, Biomed. Chromatogr. 29 (2015) 961–965, https://doi.org/10.1002/bmc.3385.
[7] R. Capuano, M. Santonico, G. Pennazza, S. Ghezzi, E. Martinelli, C. Roscioni, G. Lucantoni, G. Galluccio, R. Paolesse, C. Di Natale, A. D'Amico, The lung cancer breath signature: a comparative analysis of exhaled breath and air sampled from inside the lungs, Sci. Rep. 5 (2015) 16491, https://doi.org/10.1038/srep16491.
[8] H.J. O'Neill, S.M. Gordon, M.H. O'Neill, R.D. Gibbons, J.P. Szidon, A computerized classification technique for screening for the presence of breath biomarkers in lung cancer, Clin. Chem. 34 (1988) 1613–1618, https://doi.org/10.1016/S0009-9120(88)80010-9.
[9] P.J. Mazzone, J. Hammel, R. Dweik, J. Na, C. Czich, D. Laskowski, T. Mekhail, Diagnosis of lung cancer by the analysis of exhaled breath with a colorimetric sensor array, Thorax. 62 (2007) 565, https://doi.org/10.1136/thx.2006.072892.
[10] N. Ahmed, T. Bezabeh, O.B. Ijare, R. Myers, R. Alomran, M. Aliani, Z. Nugent, S. Banerji, J. Kim, G. Qing, Z. Bshouty, Metabolic Signatures of Lung Cancer in Sputum and Exhaled Breath Condensate Detected by 1H Magnetic Resonance Spectroscopy: A Feasibility Study, Magnetic resonance insights. 9 (2016) 29–35, https://doi.org/10.4137/MRI.S40864.
[11] J. Rudnicka, M. Walczak, T. Kowalkowski, T. Jezierski, B. Buszewski, Determination of volatile organic compounds as potential markers of lung cancer by gas chromatography–mass spectrometry versus trained dogs, Sensor Actuat B-Chem. 202 (2014) 615–621, https://doi.org/10.1016/j.snb.2014.06.006.
[12] B. Buszewski, T. Ligor, T. Jezierski, A. Wenda-Piesik, M. Walczak, J. Rudnicka, Identification of volatile lung cancer markers by gas chromatography–mass spectrometry: comparison with discrimination by canines, Anal. Bioanal. Chem. 404 (2012) 141–146, https://doi.org/10.1007/s00216-012-6102-8.
[13] M. Jang, J. Lee, S.Y. Park, J. Lee, K.M. Lee, W. Song, S. Myung, S.S. Lee, H.-K. Jung, Y.C. Kang, S.K. Kwak, K.-S. An, Rational surface modification of ZnO with siloxane polymers for room-temperature-operated thin-film transistor-based gas sensors, Appl. Sur. Sci. 542 (2021), 148704, https://doi.org/10.1016/j.apsusc.2020.148704.
[14] S. Mehmood, X. Zhao, M. Fahad Bhopal, F. Ullah Khan, Y. Yang, G. Wang, X. Pan, MoO_2-Ni-graphene ternary nanocomposite for a high- performance room-temperature ethanol gas sensor, Appl. Surf. Sci. 554 (2021), 149595, https://doi.org/10.1016/j.apsusc.2021.149595.
[15] U.T. Nakate, P. Patil, Y.T. Nakate, S.-I. Na, Y.T. Yu, Y.-B. Hahn, Ultrathin ternary metal oxide Bi_2MoO_6 nanosheets for high performance asymmetric supercapacitor and gas sensor applications, Appl. Surf. Sci. 551 (2021), 149422, https://doi.org/10.1016/j.apsusc.2021.149422.
[16] L. Lyu, Q. Xie, Y. Yang, R. Wang, W. Cen, S. Luo, W. Yang, Y. Gao, Q. Xiao, P. Zou, Y. Yang, A novel CeO_2 Hollow-Shell sensor constructed for high sensitivity of acetone gas detection, Appl. Surf. Sci. 571 (2022), 151337, https://doi.org/10.1016/j.apsusc.2021.151337.
[17] Y. Luo, A. Ly, D. Lahem, C. Zhang, M. Debliquy, A novel low-concentration isopropanol gas sensor based on Fe-doped ZnO nanoneedles and its gas sensing mechanism, J. Mater. Sci. 56 (2021) 3230–3245, https://doi.org/10.1007/s10853-020-05453-1.
[18] S. Acharyya, S. Nag, S. Kimbahune, A. Ghose, A. Pal, P.K. Guha, Selective Discrimination of VOCs Applying Gas Sensing Kinetic Analysis over a Metal Oxide-Based Chemiresistive Gas Sensor, ACS Sensors. 6 (2021) 2218–2224, https://doi.org/10.1021/acssensors.1c00115.
[19] N. Zhang, F. Xie, J. Wang, Q. Zhang, S. Zhang, L. Wang, High Throughput Screening of Surface Modificated In_2O_3 for VOC Gas Sensing Array Optimization, IEEE Sens. J. 20 (2020) 7318–7325, https://doi.org/10.1109/JSEN.2020.2970812.
[20] H. Chai, Z. Zheng, K. Liu, J. Xu, K. Wu, Y. Luo, H. Liao, M. Debliquy, C. Zhang, Stability of Metal Oxide Semiconductor Gas Sensors: A Review, IEEE Sens. J. 22 (2022) 5470–5481, https://doi.org/10.1109/JSEN.2022.3148264.
[21] B. Wang, Q. Yu, S. Zhang, T. Wang, P. Sun, X. Chuai, G. Lu, Gas sensing with yolk-shell $LaFeO_3$ microspheres prepared by facile hydrothermal synthesis, Sensor. Actuat. B: Chem. 258 (2018) 1215–1222, https://doi.org/10.1016/j.snb.2017.12.018.
[22] Y.M. Zhang, Y.T. Lin, J.L. Chen, J. Zhang, Z.Q. Zhu, Q.J. Liu, A high sensitivity gas sensor for formaldehyde based on silver doped lanthanum ferrite, Sensor. Actuat. B: Chem. 190 (2014) 171–176, https://doi.org/10.1016/j.snb.2013.08.046.
[23] J. Zhou, J. Zhang, A.U. Rehman, K. Kan, L. Li, K. Shi, Synthesis, characterization, and ammonia gas sensing properties of Co_3O_4@CuO nanochains, J. Mater. Sci. 52 (2017) 3757–3770, https://doi.org/10.1007/s10853-016-0561-9.
[24] R. Zhao, Z. Wang, T. Zou, Z. Wang, Y. Yang, X. Xing, Y. Wang, Synthesis and Enhanced Sensing Performance of g-C_3N_4/SnO_2 Composites toward Isopropanol, Chem. Lett. 47 (2018) 881–882, https://doi.org/10.1246/cl.180296.
[25] H. Aono, E. Traversa, M. Sakamoto, Y. Sadaoka, Crystallographic characterization and NO_2 gas sensing property of LnFeO(3) prepared by thermal decomposition of Ln-Fe hexacyanocomplexes, Ln[Fe(CN)(6)]center dot nH(2)O, Ln = La, Nd, Sm, Gd, and Dy, Sensor. Actuat. B-Chem. 94 (2003) 132–139, https://doi.org/10.1016/S0925-4005(03)00328-9.
[26] C. Shi, H. Qin, M. Zhao, X. Wang, L. Li, J. Hu, Investigation on electrical transport, CO sensing characteristics and mechanism for nanocrystalline $La_{1-x}CaxFeO_3$ sensors, Sensor. Actuat. B-Chem. 190 (2014) 25–31, https://doi.org/10.1016/j.snb.2013.08.029.
[27] G. Zhang, X.-Z. Song, X.-F. Wang, N. Liu, X. Li, Z. Wei, G. Qian, Z. Wang, S. Yu, Z. Tan, LnFeO(3) (Ln=La, Nd, Sm) derived from bimetallic organic frameworks for gas sensor, J. Alloy. Compd. 902 (2022), 163803, https://doi.org/10.1016/j.jallcom.2022.163803.
[28] M. Siemons, A. Leifert, U. Simon, Preparation and gas sensing characteristics of nanoparticulate p-type semiconducting LnFeO(3) and LnCrO(3) materials, Adv. Funct. Mater. 17 (2007) 2189–2197, https://doi.org/10.1002/adfm.200600454.
[29] Y. Huan, K. Wu, C. Li, H. Liao, M. Debliquy, C. Zhang, Micro-nano structured functional coatings deposited by liquid plasma spraying, J Adv Ceram. 9 (2020) 517–534, https://doi.org/10.1007/s40145-020-0402-9.
[30] Y. Cao, C. Zhou, H. Qin, J. Hu, High-performance acetone gas sensor based on ferrite-$DyFeO_3$, J. Mater. Sci. 55 (2020) 16300–16310, https://doi.org/10.1007/s10853-020-05194-1.
[31] T.T. Yang, S.Y. Ma, P.F. Cao, X.L. Xu, L.i. Wang, S.T. Pei, T. Han, X.H. Xu, P.D. Yun, H. Sheng, Synthesis and characterization of $ErFeO_3$ nanoparticles by a hydrothermal method for isopropanol sensing properties, Vacuum. 185 (2021), 110005, https://doi.org/10.1016/j.vacuum.2020.110005.
[32] H. Sheng, S. Ma, T. Han, P. Yun, T. Yang, J. Ren, A highly sensitivity and anti-humidity gas sensor for ethanol detection with $NdFeO_3$ nano-coral granules, Vacuum. 195 (2022), 110642, https://doi.org/10.1016/j.vacuum.2021.110642.
[33] F. Yang, L. Guo, P. Li, X. Zhao, Y. Sui, Z. Guo, X. Gao, Boundary structure modification and magnetic properties of Nd-Fe-B sintered magnets by co-doping with Dy_2O_3/S powders, J. Magn. Magn. Mater. 429 (2017) 117–123, https://doi.org/10.1016/j.jmmm.2017.01.029.
[34] M. Alam, I. Chakraborty, K. Mandal, Microwave synthesis of surface functionalized $ErFeO_3$ nanoparticles for photoluminescence and excellent photocatalytic activity, J. Lumin. 196 (2018) 387–391, https://doi.org/10.1016/j.jlumin.2017.12.057.
[35] J. Shanker, G.N. Rao, K. Venkataramana, D.S. Babu, Investigation of structural and electrical properties of $NdFeO_3$ perovskite nanocrystalline, Phys. Lett. A. 382 (2018) 2974–2977, https://doi.org/10.1016/j.physleta.2018.07.002.
[36] P.P. Ortega, C.C. Silva, M.A. Ramirez, G. Biasotto, C.R. Foschini, A.Z. Simões, Multifunctional environmental applications of ZnO nanostructures synthesized by the microwave-assisted hydrothermal technique, Appl. Surf. Sci. 542 (2021), 148723, https://doi.org/10.1016/j.apsusc.2020.148723.
[37] S. Meti, M.R. Rahman, M.I. Ahmad, K.U. Bhat, Chemical free synthesis of graphene oxide in the preparation of reduced graphene oxide-zinc oxide nanocomposite with improved photocatalytic properties, Appl. Surf. Sci. 451 (2018) 67–75, https://doi.org/10.1016/j.apsusc.2018.04.138.
[38] M.K. Kavitha, H. John, P. Gopinath, R. Philip, Synthesis of reduced graphene oxide–ZnO hybrid with enhanced optical limiting properties, J. Mater. Chem. C. 1 (2013) 3669–3676, https://doi.org/10.1039/C3TC30323C.
[39] L. Xu, W. Zeng, Y. Li, Synthesis of morphology and size-controllable SnO_2 hierarchical structures and their gas-sensing performance, Appl. Surf. Sci. 457 (2018) 1064–1071, https://doi.org/10.1016/j.apsusc.2018.07.018.
[40] L. Man, J. Zhang, J. Wang, H. Xu, B. Cao, Microwave-assisted hydrothermal synthesis and gas sensitivity of nanostructured SnO_2, Particuology. 11 (2013) 242–248, https://doi.org/10.1016/j.partic.2012.01.005.
[41] A. Mirzaei, G. Neri, Microwave-assisted synthesis of metal oxide nanostructures for gas sensing application: A review, Sensor Actuat B-Chem. 237 (2016) 749–775, https://doi.org/10.1016/j.snb.2016.06.114.
[42] Y. Li, Y.-L. Lu, K.-D. Wu, D.-Z. Zhang, M. Debliquy, C. Zhang, Microwave-assisted hydrothermal synthesis of copper oxide-based gas-sensitive nanostructures, Rare Met. 40 (2021) 1477–1493, https://doi.org/10.1007/s12598-020-01557-4.

[43] Y. Yin, N. Zhang, J. Han, C. Liu, S. Adimi, S. Wen, X. Li, S. Ruan, Metal-organic framework derived core-shell $PrFeO_3$-functionalized alpha-Fe_2O_3 nano-octahedrons as high performance ethyl acetate sensors, Sensor. Actuat. B-Chem. 297 (2019), 126738, https://doi.org/10.1016/j.snb.2019.126738.
[44] P. Chen, L. Jiang, S. Yang, H. Chen, J. He, Y. Wang, J. An, Effects of combustion agents on the synthesis of perovskite erbium ferrite ($ErFeO_3$) nanocrystalline powders fabricated by auto-propagating combustion process, Inorg. Chem. Commun. 101 (2019) 164–171, https://doi.org/10.1016/j.inoche.2019.01.028.
[45] L. Sun, J. Hu, H. Qin, M. Zhao, K. Fan, Influences of Ca Doping and Oxygen Vacancy upon Adsorption of CO on the $LaFeO_3$ (010) Surface: A First-Principles Study, J. Phys. Chem. C. 115 (2011) 5593–5598, https://doi.org/10.1021/jp107038z.
[46] L. Li, M. Zhang, P. Tian, W. Gu, X. Wang, Synergistic photocatalytic activity of LnFeO(3) (Ln = Pr, Y) perovskites under visible-light illumination, Ceram Int. 40 (2014) 13813–13817, https://doi.org/10.1016/j.ceramint.2014.05.097.
[47] P. Shikha, T.S. Kang, B.S. Randhawa, Effect of different synthetic routes on the structural, morphological and magnetic properties of Ce doped $LaFeO_3$ nanoparticles, J. Alloy. Compd. 625 (2015) 336–345, https://doi.org/10.1016/j.jallcom.2014.11.074.
[48] H. Xu, J. Xu, J. Wei, Y. Zhang, Fast response isopropanol sensing properties with sintered $BiFeO_3$ nanocrystals, Materials. 13 (17) (2020), 3829, https://doi.org/10.3390/ma13173829.
[49] D. Hu, B. Han, R. Han, S. Deng, Y. Wang, Q. Li, Y. Wang, SnO_2 nanorods based sensing material as an isopropanol vapor sensor, New J. Chem. 38 (2014) 2443–2450, https://doi.org/10.1039/C3NJ01482G.
[50] H. Zhang, Z. Jin, M.D. Xu, Y. Zhang, J. Huang, H. Cheng, X.F. Wang, Z.L. Zheng, Y. Ding, Enhanced Isopropanol Sensing Performance of the CdS Nanoparticle Decorated ZnO Porous Nanosheets-Based Gas Sensors, IEEE Sensors J. 21 (2021) 13041–13047, https://doi.org/10.1109/JSEN.2021.3054654.
[51] E.S. Guillén-López, F. López-Urías, E. Muñoz-Sandoval, M. Courel-Piedrahita, M. Sanchez-Tizapa, H. Guillén-Bonilla, V.M. Rodríguez-Betancourtt, O. Blanco-Alonso, A. Guillén-Bonilla, J.P. Morán-Lázaro, High performance isopropanol sensor based on spinel $ZnMn_2O_4$ nanoparticles, Materials Today Communications. 26 (2021), 102138, https://doi.org/10.1016/j.mtcomm.2021.102138.
[52] D. Hu, B. Han, S. Deng, Z. Feng, Y. Wang, J. Popovic, M. Nuskol, Y. Wang, I. Djerdj, Novel Mixed Phase SnO2 Nanorods Assembled with SnO2 Nanocrystals for Enhancing Gas-Sensing Performance toward Isopropanol Gas, J. Phys. Chem. C. 118 (2014) 9832–9840, https://doi.org/10.1021/jp501550w.
[53] M.K. Sohal, A. Mahajan, S. Gasso, S.V. Nahirniak, T.A. Dontsova, R.C. Singh, Rare earth-tuned oxygen vacancies in gadolinium-doped tin oxide for selective detection of volatile organic compounds, J. Mater. Sci.: Mater. Electron. 31 (2020) 8446–8455, https://doi.org/10.1007/s10854-020-03379-7.
[54] C. Zhang, Y. Huan, Y. Li, Y. Luo, M. Debliquy, Low concentration isopropanol gas sensing properties of Ag nanoparticles decorated In_2O_3 hollow spheres, J. Adv. Ceramics. 11 (2022) 379–391, https://doi.org/10.1007/s40145-021-0530-x.
[55] T.T. Yang, S.Y. Ma, P.F. Cao, X.L. Xu, L. Wang, S.T. Pei, T. Han, X.H. Xu, P.D. Yun, H. Sheng, Synthesis and characterization of $ErFeO_3$ nanoparticles by a hydrothermal method for isopropanol sensing properties, Vacuum. 185 (2021), 110005, https://doi.org/10.1016/j.vacuum.2020.110005.
[56] Y. Yao, Y. Han, M. Zhou, L. Xie, X. Zhao, Z. Wang, N. Barsan, Z. Zhu, $MoO_3/TiO_2/Ti_3C_2T_x$ nanocomposite based gas sensors for highly sensitive and selective isopropanol detection at room temperature, J. Mater. Chem. A. 10 (2022) 8283–8292, https://doi.org/10.1039/D1TA11018G.
[57] G. Wang, P. Wu, L. Guo, W. Wang, W. Liu, Y. Wang, T. Chen, H. Wang, Y. Xu, Y. Yang, Preparation of Au@ZnO nanofilms by combining magnetron sputtering and post-annealing for selective detection of isopropanol, Chemosensors. 10 (6) (2022) 211, https://doi.org/10.3390/chemosensors10060211.
[58] N. Jayababu, M. Poloju, J. Shruthi, M.V.R. Reddy, NiO decorated CeO_2 nanostructures as room temperature isopropanol gas sensors, RSC Advances. 9 (2019) 13765–13775, https://doi.org/10.1039/C9RA00441F.
[59] B. Zhang, W. Fu, X. Meng, R. A, P. Su, H. Yang, Synthesis of actinomorphic flower-like SnO_2 nanorods decorated with CuO nanoparticles and their improved isopropanol sensing properties, Appl. Surf. Sci. 456 (2018) 586–593, https://doi.org/10.1016/j.apsusc.2018.06.150.
[60] C. Zhang, Y. Li, G.-F. Liu, H.-L. Liao, Preparation of ZnO_{1-x} by peroxide thermal decomposition and its room temperature gas sensing properties, Rare Met. 41 (2022) 871–876, https://doi.org/10.1007/s12598-021-01840-y.
[61] H. Sheng, S. Ma, T. Han, P. Yun, T. Yang, J. Ren, A highly sensitivity and anti-humidity gas sensor for ethanol detection with $NdFeO_3$ nano-coral granules, Vacuum. 195 (2022) 11042, https://doi.org/10.1016/j.vacuum.2021.110642.
[62] D. Meena, B. Singh, A. Anand, M. Singh, M.C. Bhatnagar, Phase dependent selectivity shifting behavior of Cd_2SnO_4 nanoparticles based gas sensor towards volatile organic compounds (VOC) at low operating temperature, J. Alloy. Compd. 820 (2020), 153117, https://doi.org/10.1016/j.jallcom.2019.153117.
[63] X. Fan, Y. Xu, C. Ma, W. He, In-situ growth of Co_3O_4 nanoparticles based on electrospray for an acetone gas sensor, J. Alloy. Compd. 854 (2021), 157234, https://doi.org/10.1016/j.jallcom.2020.157234.
[64] C. Zhang, K. Wu, H. Liao, M. Debliquy, Room temperature WO_3-Bi_2WO_6 sensors based on hierarchical microflowers for ppb-level H_2S detection, Chem. Eng. J. 430 (2022), 132813, https://doi.org/10.1016/j.cej.2021.132813.
[65] K.-D. Wu, J.-Y. Xu, M. Debliquy, C. Zhang, Synthesis and NH_3/TMA sensing properties of $CuFe_2O_4$ hollow microspheres at low working temperature, Rare Metals. 40 (2021) 1768–1777, https://doi.org/10.1007/s12598-020-01609-9.